Title

Ultrafast timing enables reconstruction-free positron emission imaging

Authors

Kwon, Sun Il
Ota, Ryosuke
Berg, Eric
et al.

Peer reviewed

Ultrafast timing enables reconstruction-free positron emission imaging

Sun Il Kwon[1,*], **Ryosuke Ota**[2,*], **Eric Berg**[1,*], **Fumio Hashimoto**[2], **Kyohei Nakajima**[3], **Izumi Ogawa**[3], **Yoichi Tamagawa**[3], **Tomohide Omura**[2], **Tomoyuki Hasegawa**[4], **Simon R. Cherry**[1]

[1]Department of Biomedical Engineering, University of California; Davis, USA

[2]Central Research Laboratory, Hamamatsu Photonics K.K.; Hamamatsu, Japan

[3]Faculty of Engineering, University of Fukui; Fukui, Japan

[4]School of Allied Health Sciences, Kitasato University; Kitasato, Japan

Abstract

X-ray and gamma-ray photons are widely used for imaging but require a mathematical reconstruction step, known as tomography, to produce cross-sectional images from the measured data. Theoretically, the back-to-back annihilation photons produced by positron-electron annihilation can be directly localized in three-dimensional space using time-of-flight information without tomographic reconstruction. However, this has not yet been demonstrated due to the insufficient timing performance of available radiation detectors. Here, we develop techniques based on detecting prompt Cerenkov photons, which when combined with a convolutional neural network for timing estimation resulted in an average timing precision of 32 picoseconds, corresponding to a spatial precision of 4.8 mm. We show this is sufficient to produce cross-sectional images of a positron-emitting radionuclide directly from the detected coincident annihilation photons, without using any tomographic reconstruction algorithm. The reconstruction-free imaging demonstrated here directly localizes positron emission, and frees the design of an imaging system from the geometric and sampling constraints that normally present for tomographic reconstruction.

Three-dimensional biomedical imaging techniques including x-ray computed tomography (CT) single photon emission computed tomography (SPECT) and positron emission tomography (PET) measure one-dimensional or two-dimensional projections from the object of interest that subsequently are reconstructed into cross-sectional images or 3-D image volumes via analytic computed tomography algorithms based on the Radon transform[1], or using iterative algorithms, typically based on the expectation-maximization algorithm[2]. In

magnetic resonance imaging (MRI), data are natively acquired in the frequency domain and are subsequently reconstructed into images in the spatial domain through the Fourier transform[3]. In all these imaging modalities, a measured data point does not have a 1:1 correspondence with a point in image space, and the spatial distribution of the signal must be inferred by a reconstruction step. Accurate tomographic image reconstruction also depends on adequate angular (PET, SPECT and CT) or frequency (MRI) sampling of the data.

Uniquely among these imaging modalities, PET can localize the signal source beyond the entire line of response by exploiting the time difference in detection of the two back-to-back annihilation photons produced following the emission of a positron (Fig. 1)[4]. This is the basis for time-of-flight PET (Fig. 1a), and the best systems currently available have a timing resolution of ~210 ps[5] resulting in a spatial localization along the line of response of 3.15 cm. As shown in Fig. 1c, this constrains the possible location of a detected event, but does not define the source location, and therefore image reconstruction with all its concomitant limitations is still required. The propagation of noise from the reconstruction algorithm, and the predicted improvements in image signal-to-noise ratio (SNR) as a function of time-of-flight resolution, have been previously studied as summarized by Budinger[6].

Once the timing resolution becomes sufficiently good enough to directly localize the source, we enter a new regime, in which an image can be directly obtained without any reconstruction step. We call this direct positron emission imaging (dPEI) (Fig. 1d). This approach is somewhat analogous to ultrasound, which also uses time-of-flight differences, at the speed of sound in tissue, to localize the depth of ultrasound-reflections. However, in dPEI, the time-of-flight differences are governed by the speed of light rather than the speed of sound, resulting in time differences of tens of ps rather than μs. In this work we developed very fast radiation detectors, with an average coincidence timing resolution of 32 ps, and demonstrate, for the first time, the generation of cross-sectional images of the distribution of a positron-labeled radiotracer while completely eliminating the noise-amplifying image reconstruction algorithm. Here, we describe the enabling technological and methodological innovations, measure the timing performance and the relationship between the source localization and the measured time-of-flight difference, and show cross-sectional images of three different test objects, produced directly from a single angular view without tomographic image reconstruction.

Fast time-of-flight radiation detectors used for imaging positron-emitting radionuclides normally consist of a bright, high-density scintillator coupled to a silicon photomultiplier (SiPM) that electronically converts and amplifies the scintillation light through the generation of electron-hole pairs and the use of a high electric field[7]. However, the rate at which photons are produced by the scintillation process is relatively slow, due to the time needed to form excited states and for recombination to occur[8]. Furthermore, silicon photomultipliers have a single photon time resolution (SPTR) that is typically on the order of 100-300 ps[9,10]. Therefore, to achieve timing resolutions of 40 ps or better needed for dPEI likely requires a different strategy. Various approaches have recently been discussed as part of an international challenge launched to focus efforts on ultimately achieving 10 ps timing resolution[4]. In this work we combined three innovations to make dPEI possible, namely the use of Cerenkov luminescence as the mechanism to achieve a fast timing

signal, the integration of a Cerenkov radiator directly within the photosensor to optimize light transport and photodetection timing properties, and the application of convolutional neural network (CNN) as a standalone algorithm to predict the timing information from the measured detector waveforms.

Cerenkov radiation is produced when a charged particle travels faster than the phase velocity of light in a medium, is emitted promptly, and therefore presents as an attractive mechanism to be exploited for ultra-fast timing applications[11,12]. The detection of 511 keV photons emitted following positron-electron annihilation in materials with high refractive index and high atomic number create sufficiently energetic electrons to produce a small number of Cerenkov photons[13–15]. Next, this prompt optical signal needs to be converted to an electronic signal and amplified, and for this we developed a photosensor based on the structure of microchannel plates (MCP). MCP photomultiplier tubes (MCP-PMTs) are known for their outstanding SPTR, with values that can approach 20 ps[16]. For this work, we developed an MCP-PMT in which the Cerenkov radiator (lead glass) was integrated with the photocathode inside the MCP-PMT (Fig. 2a), thus removing all optical boundaries that had hampered detection of the Cerenkov photons and reduced detection[17]. These devices are henceforth referred to as Cerenkov radiator integrated MCP-PMTs or CRI-MCP-PMTs. We also further refined the design by removing lead-based compounds from the MCP structure to reduce the probability of direct interactions of the 511 keV photons which leads to side peaks in the timing spectrum and ultimately results in ambiguous localization for a small percentage of detected events[18]. Lastly, we used a CNN to determine the time of flight difference for detected events, extending previously developed methods[19]. By placing radioactive point sources at different locations between a detector pair, large numbers ($>10^6$) of training events with known ground truth time-of-flight differences can readily be collected for training, allowing the CNN to learn the complex waveforms and output the time-of-flight difference. The CNN is a 9-layer network where each layer contains convolution, batch normalization, and a rectified linear activation function. The whole CNN was trained using stochastic gradient descent.

All data was acquired using two CRI-MCP-PMTs, placed in coincidence, with lead or tungsten collimation of the 11 mm diameter active area of the photocathode based on the desired image resolution. After optimizing the bias voltages supplied to the different stages of the CRI-MCP-PMTs the estimated SPTR was 22 ps, and the gain was ~1.8×10^6 when a bias voltage of −3.0 kV was supplied. The CRI-MCP-PMT has the same quantum efficiency (QE) curve as the R3809U-50 MCP-PMT (Hamamatsu Photonics K.K., Japan) with a QE above 20% for the wavelength range 200-420 nm. Fig. 2b shows a histogram of the time of flight differences for a point source of ^{22}Na located at the center of a detector pair. The measured coincidence timing resolution (calculated as the full width at half maximum (FWHM) of the timing distributions based on constant fraction timing of the digitized waveforms was 32.9 ps, improving to 26.4 ps by using the CNN. The corresponding full width at tenth maximum of the distributions were 86.4 ps and 68.0 ps, respectively. Fig. 2c shows the time-of-flight histograms for 5 source locations, spaced by 25 mm, demonstrating the linear relationship between the measured time-of-flight different and source location (also see Extended Data Fig. 1), as well as the relatively uniform timing resolution achieved

across a 10 cm range (26.4 – 35.7 ps). The corresponding spatial resolution was 3.96 mm at the center, and was better than 5.36 mm across the entire range.

Imaging studies were performed in three different test objects filled with an aqueous solution of the radiotracer ^{18}F-fluorodeoxyglucose (^{18}F-FDG) ($T_{1/2}$=110 mins.). To capture images, the detector pair was translated linearly to cover the width of the object, building up the image one row of pixels at a time (Fig. 3). The acquisition duration at each position was adjusted for radioactive decay to provide roughly equal counting statistics for each measurement. Images were generated directly from the measured data without any reconstruction, using the position of the detector pair to determine the *x*-coordinate and the time-difference of the two detected events to determine the *y*-coordinate. No rotation of the object or detectors was required to form a cross-sectional image. Fig. 3c shows the first dPEI image produced. The small number of detected events that occur outside the boundaries of the object are a result of direct interactions in, or photoelectron backscatter from, the MCP structure[18]

Figure 4 shows the images for each of the test objects using the CNN to determine the timing difference on an event-by-event basis, and correcting for radioactive decay, acquisition time, and attenuation of the 511 keV photons by the object based on analytic calculations. Each of the test objects highlights a different imaging attribute or task. The first object (Fig. 4a) is commonly used as an image quality test in preclinical PET scanners and consists of a uniform background with two voids where there is no activity, one filled with air, and one filled with water. Both voids, which are 8 mm in diameter, are clearly visualized. The second object is a resolution test pattern with radioactive rods of different diameters and a spacing equal to twice their diameters (Fig. 4b). The image demonstrated that the 3 mm rods can be resolved, indicating that a spatial resolution on the order of 4-5 mm is recovered in the dPEI images in line with expectations based on the average measured timing response of 32 ps. The third object is much larger (18.4 cm in diameter) and represents the distribution of FDG in a slice of the human brain (Fig. 4c). The detailed structure in this object is faithfully captured in the dPEI image with a spatial resolution of ~4.8 mm and demonstrates that the method could be scaled for human imaging.

These images represent the first examples of the direct localization and imaging of a positron-emitting radionuclide, using data from a single angular view and without any tomographic image reconstruction algorithm, to generate a cross-sectional image. This two-detector system with its average timing resolution of 32 ps was able to produce images at a spatial resolution of 4.8 mm in the timing direction. This spatial resolution is already similar to that achieved in images from TOF-PET scanners used for diagnostic purposes. The spatial resolution in the *x*-direction (direction of translation, see Fig. 3a) is roughly one-half the collimated detector width. 3D volumetric images could in principle be acquired by also translating the detector pair in the *z* direction.

A number of limitations must be addressed in order to develop more practical dPEI systems. The acquisition times in these first imaging experiments were long (2-34 minutes per measurement position, 4-24 hours for the whole image) and the amount of radioactivity used high (up to ~1000 MBq). This initial demonstration of the principles of dPEI and

its implementation should be viewed from the same standpoint as the earliest computed tomography experiments by Hounsfield that yielded the first cross-sectional images[20]. These experiments involved a radiation source (either a radioactive source or an x-ray tube), and radiation detector that were translated, and also rotated, to produce the necessary projection data for CT reconstruction. Acquisition times were initially as long as 9 days. Now, of course, CT scans of a large volume of tissue can be accomplished at low radiation doses in well under a second.

There are obvious avenues to increase signal collection efficiency to achieve large reductions in time and dose. These include using a higher atomic number radiator (such as the scintillator bismuth germanate, which produces both Cerenkov and scintillation light) in place of the lead glass radiator used in these MCP-PMTs, increasing the thickness of the radiator to 4-5 mm, developing multi-channel detectors that can be tiled together, and then using multiple detectors arranged in linear arrays or panels to increase geometric coverage allowing large numbers of photon paths through the object to be measured simultaneously. These three changes alone could increase the detection sensitivity by $>10^3$, reducing acquisition times or radiation doses accordingly. This would allow the time required to acquire the data used to generate the brain phantom image shown in Fig. 4c to be reduced from 24 hours to only ~1 minute. Multi-detector configurations that cover the imaging volume of interest would also remove the need for detector translation and allow dynamic imaging of radiotracer distributions.

dPEI as a novel imaging modality offers a number of interesting opportunities, by freeing the design of the imaging system from the typical constraints associated with the sampling necessary for tomographic reconstruction. For example, dPEI systems need only cover the region of an object that is of interest, as truncation artifacts, which are prevalent in tomography, are no longer an issue. Also, in the medical setting, systems need not consist of complete detector rings that enclose a subject, but can allow a more open geometry for improved access to, and acceptance by, patients, while still providing fully 3D images. In addition, because each individual event carries the information needed to completely localize it in 3D space, the image signal-to-noise ratio is maximized for a given number of detected events. This is exemplified by Fig. 4, where each image is comprised of just 4,000 – 20,000 events, yet this is sufficient to clearly visualize the object (see Extended Data Fig. 2). Once larger scale systems, with more efficient detectors are developed, it should be possible for dPEI to acquire high SNR images at low radiation doses and with short acquisition times. Furthermore, dPEI opens up the possibility of real-time imaging, as no reconstruction step is involved and images can be viewed as they are in the process of being acquired.

Methods:

Timing simulations

Monte Carlo simulation studies were conducted to illustrate the differences in the probability distribution for source locations in coincidence event detection comparing positron emission tomography (PET), PET with time-of-flight capability (TOF-PET), and direct positron emission imaging (dPEI). GATE version 9.0 software[21,22], which is based on the GEANT 4 simulation platform, was used. In the simulation studies, two radiation detectors were

arranged face-to-face with a separation of 96 mm (Fig. 1a). The active area of each detector was 9.6×9.6 mm^2. The volume between the two detectors ($9.6 \times 9.6 \times 96$ mm^3) was uniformly filled with 1 MBq of activity, with the source being defined as an ideal back-to-back 511-keV mono-energetic emitter in air. A total of approximately 31 million coincidence events were acquired, with each event containing information about the source location and the interaction position on each detector surface.

The difference in arrival time of two photons in each coincidence event was calculated using the recorded source position and the two detected positions. For display purposes, the 2-D probability distribution of the estimated source locations on the xy-plane was calculated from the 3-D distribution by integrating the probability maps along the z-direction. For PET alone (Fig. 1b), where no timing information is available, the distribution is governed by coincidence detection geometry alone. For TOF-PET (Fig. 1c), the 2-D probability distribution was calculated by applying Gaussian weighting in the time domain with a timing resolution of 210 ps full-width at half-maximum (FWHM), which models the best-reported timing resolution for a commercial TOF-PET system (4). In the case of dPEI imaging, Gaussian weighting with a timing resolution of 32 ps FWHM, which models the timing performance measured for the dPEI system used in this study, was applied in the time domain. For the right-hand column of Fig. 1 where three adjacent sources were modeled, we applied: i) no time domain weighting for standard PET imaging, ii) three Gaussian weightings centered on the source location each with the same timing resolution of 210 ps FWHM for TOF PET imaging, and iii) three Gaussian weightings with 32 ps FWHM for dPEI imaging.

Cerenkov radiator integrated MCP-PMT

A pair of microchannel plate photomultiplier tubes (MCP-PMTs), in which a lead glass Cherenkov radiator was integrated as the window face plate of the MCP-PMTs (referred to as CRI-MCP-PMTs), were designed, fabricated and used to detect 511 keV photons in coincidence with ultra-high timing resolution. The dimensions of each MCP-PMT are 45 mm in diameter and 52.5 mm length, with an active detection area 11 mm in diameter (Fig. 2a). The lead glass window face plate is 3.2 mm thick and has a 511 keV photon cross-section of 0.43 cm^{-1}, resulting in an expected detection efficiency of 12.9% (1.65% in coincidence). The lead glass radiator has a refractive index of ~1.5 which leads to a calculated Cerenkov light yield of ~8.7 photons (350-750 nm range) per 511 keV photoelectric absorption and an experimentally estimated yield of ~2.8 photons averaged across all 511 keV photon interactions[18]. The peak quantum efficiency of the CRI-MCP-PMT is ~21% at 430 nm. The MCP incorporated in the PMT structure consisted of borosilicate glass fabricated through an atomic layer deposition (ALD) technique that replaced conventional lead-based compounds to reduce the probability of 511 keV photons directly interacting within the MCP structure, instead of the Cerenkov radiator window faceplate. Such directly interacting events would otherwise degrade timing performance[23]. A multialkali photocathode was deposited on the lead glass Cerenkov radiator via a 2-3 nm thick Al_2O_3 intermediate layer to protect against chemical reactions occurring between the lead glass and the photocathode when using the ALD technique.

To optimize the intrinsic timing performance of the MCP-PMTs, a custom voltage divider circuit was employed to tune the photoelectron gain across the MCP-PMT. Resistors of 7.5 MΩ, 18 MΩ, and 15 MΩ were selected between the photocathode and MCP_{in}, MCP_{in} and MCP_{out}, and MCP_{out} and the anode, respectively (Fig. 2a). A voltage of −3.0 kV was supplied to the photocathode of each MCP-PMT. The entrance surface of the MCP-PMT was covered by black tape to suppress internal optical reflections in the radiator to further optimize the detector's timing performance.

Experiments at Hamamatsu Photonics K.K.

Initial experiments were performed independently at both the Central Research Laboratory, Hamamatsu Photonics, Japan, and the University of California, Davis (UC Davis) to ensure reproducibility of the results. Experimental conditions for the CRI-MCP-PMT detectors (detector modules used, divider circuit, supplied bias voltage, black tape) were identical for both experimental sites, while there were minor differences in experimental setups used due to equipment and materials available. An overview of both experimental setups is shown in Supplementary Data Fig. 1. A 50 mm thick lead collimator with 2 mm opening width was used for the experiments at Hamamatsu Photonics, K.K., Japan. The NEMA NU4 image quality phantom (Fig. 4d and Supplementary Data Fig. 2a), a standardized object used for testing PET imaging systems[24], was fixed on a linear translation stage (SGSP20-35, Sigma Koki, Japan) and motorized by a stage controller (SHOT-102, Sigma Koki, Japan).

The NEMA-NU4 phantom was filled with 9 mL of ^{18}F-NaF in aqueous solution and with an initial activity concentration in the background region of 227 MBq/ml (2.04 GBq total activity), as measured by a well counter (IGC-7, Aloka, Japan). One of the 8-mm inner diameter voids was filled with water, the other was filled with air. The phantom was stepped laterally across its width in 0.5 mm increments. 70 timing spectra covering 3.5 cm were collected in total.

Signals from the MCP-PMTs were directly fed into an oscilloscope (DSOS404A, Keysight, USA) and digitized at 20 GS/s with a bandwidth of 4.2 GHz. Waveforms were fully digitized on an event-by-event basis, and transferred to a personal computer for analysis. The trigger time difference ($t_A - t_B$) between the two digitized signals for each event was calculated and used to estimate the location of positron annihilation. The threshold level for the triggering each signal was set to 4% of the pulse height of the signal. The total duration of data acquisition was ~5.5 hours and the acquisition duration at each location was gradually increased from 2 mins to 15.6 mins to account for ^{18}F decay (half-life = 110.9 minutes). The timing spectrum obtained for one specific measurement location is shown in Fig. 3b and the final raw image data produced from this scan is shown in Fig. 3d.

Experiments at UC Davis

The same two CRI-MCP-PMTs that were used in the study at Hamamatsu Photonics K.K. were transferred to UC Davis for comparative dPEI imaging studies of the same NU4 image quality phantom, along with several additional evaluations of their timing performance and extended imaging experiments on different test objects. The two CRI-MCP-PMT detectors were mounted on top of an optical breadboard (Thorlabs Inc., USA) with their line-of-

response parallel to the *y*-axis. The custom holders for the two detectors were 3-D printed for precise alignment. In front of each detector, a custom adjustable tungsten collimator was fastened in front of each detector face, consisting of four 3.81 cm thick tungsten alloy cubes (Midwest Tungsten Service, USA). The four cubes were positioned such that their relative offsets determined the collimator height (slice thickness) along the *z*-axis, and width along the *x*-axis (Supplementary Data Fig. 1b). The distance between the two detectors and the opening area of each collimator were varied depending on the object being imaged. A bias voltage of −3 kV was applied to each detector. The output signals output from the CRI-MCP-PMTs were digitized with an oscilloscope (DPO71254C, Tektronix, USA) at a sampling rate of 50 GS/s and with a bandwidth of 12.5 GHz. Coincidence events were determined by a sequential logic triggering function in the oscilloscope using cables with different lengths.

Measurements and datasets

Four sets of experimental data were acquired at UC Davis.

1) Point source experiments: The purpose of this measurement was to characterize i) the relationship between measured time-of-flight differences and source location and ii) the coincidence timing resolution corresponding to the spatial resolution of the detector pair along the *y*-direction (see Fig. 3a for coordinate system). Coincidence events were acquired from a ^{22}Na radioactive point source placed at 5 different source locations spaced by 25 mm along the detector line-of-response (*y*-axis). The distance between the two detectors was 300 mm, and the opening area of each collimator was 8 mm (*x*-direction) and 10-mm (*z*-direction). The point source activity was 4.1 MBq, and the acquisition duration at each point source position was ~3 hours to ensure collection of sufficient counting statistics.

2) dPEI scan of the NEMA NU-4 image quality phantom: A 1-D motorized translation stage (Velmex Inc., USA) was mounted on top of the optical breadboard between the two stationary detectors to scan test objects relative to the detector pair along the *x*-direction. The NEMA NU-4 image quality phantom was prepared (Figs. 4d and Supplementary Data Fig. 2a) similarly as described previously. The 30-mm inner diameter uniform background region was filled with 847 MBq of the radiotracer ^{18}F-fluorodeoxyglucose (FDG) in aqueous solution. The phantom was scanned using the custom 3-D printed holder shown in Supplementary Data Fig. 1b to ensure accurate location and alignment. The distance between two detectors was set to 200 mm, and the opening area of each collimator was set to 2 mm (*x*-direction) and 10-mm (*z*-direction). The phantom was imaged by stepping along the *x*-direction 35 times with a 1-mm step size. The duration of data acquisition at each position was adjusted to account for ^{18}F decay: the acquisition duration at the first *x*-position was 3.56 mins, and increased up to 15.1 mins for the last position. The total acquisition time to acquire the entire dPEI image was 4 hours.

3) dPEI scan of a spatial resolution phantom: A spatial resolution test phantom (also known as a Derenzo phantom) was fabricated from acrylic. The 102-mm outer-diameter phantom consisted of 6 sectors, each sector was composed of multiple 9.53-mm tall rods with triangular equilateral spacing equal to twice the rod diameter. The rod

diameters were 2, 3, 4, 5, 6, and 7 mm, respectively (Fig. 4d and Supplementary Data Fig. 2b). Each rod was filled with ^{18}F-FDG using a syringe, and the total activity was 1,025 MBq. The distance between two detectors was 200 mm, and the opening area of each collimator was 2 mm (*x*-direction) by 10-mm (*z*-direction). The phantom was imaged by stepping along the *x*-direction 82 times with a 1-mm step size. Since the phantom size was larger than the image quality phantom, the acquisition time at the first *x*-position was reduced to 1.85 mins and the total scan time to cover the entire phantom area was 8 hours.

4) dPEI scan of the 2-D Hoffman brain phantom: A 2-D Hoffman brain phantom (Data Spectrum, USA) which represents the distribution of the radiotracer ^{18}F-FDG in the human brain was imaged (Fig. 4d). The phantom has a diameter of 184 mm and a maximum water-fillable thickness of 13 mm. Regional contrast differences (gray matter:white matter:ventricle ratio = 4:1:0) are created through partial volume effects according to the slice thickness. To scan this large brain phantom, the distance between the two detectors was increased to 300 mm, and the collimator opening width was set to 8 mm (*x*-direction) and 10-mm (*z*-direction). The phantom was filled with ~850 MBq of ^{18}F-FDG and was imaged by stepping along the *x*-direction 44 times with a 4-mm step size. The first acquisition time was 3.27 mins, and all other acquisition times were increased to adjust for ^{18}F decay so that similar counting statistics were achieved in each measurement. For the last measurement position the acquisition time was 28.6 mins. The total scan time was 6 hours. We repeated this scan eight times by re-filling the phantom with radioactivity and carefully re-positioning it inside the imaging setup to study the effect of increasing the number of collected events. The image shown in Figure 4d represents a total imaging time of 24 hours (the sum of four 6-hour acquisitions) and contains ~20,000 events.

Timing methods:

The difference in arrival time of the two annihilation photons was determined on an event-by-event basis by the trigger time difference (t_A−t_B) between the two digitized signals. The detection threshold was set at the single photon level. In the point source experiments, the trigger time difference of each signal pair was calculated using two different timing methods. The first method was the constant fraction discrimination (CFD) method, which is a conventional method to compute the trigger time of each signal and was implemented in software with parameters of a 0.3 fraction and a 110-ps delay.

For the second method, an alternative to the CFD method was developed to estimate the time-of-flight differences using a convolutional neural network (CNN)[25]. In this method, the CNN was trained to estimate time-of-flight for each coincidence event directly from the pair of digitized waveforms[19]. Here, a 9-layer CNN (Supplementary Data Fig. 3, full CNN architecture provided in Supplementary Data Table 1) was trained for TOF estimation using MATLAB with approximately 1 million coincidence events and stochastic gradient descent with momentum. The training dataset consisted of events measured from a centrally located ^{22}Na point source, shifted by random timing delays. Layer weights were initialized using He initialization[26]. Complete training parameters for the CNN are provided in Supplementary Data Table 2. Each trigger time difference (t_A−t_B) respectively computed by the CFD and CNN methods was histogrammed to form a timing spectrum. The FWHM of each timing

spectrum was obtained by linear interpolation of the data points and represented as the coincidence timing resolution.

After comparing the results of the point source experiments using CFD and CNN methods (Fig. 2b), we selected the CNN method to apply to the acquired image phantom data. For timing estimation using the trained CNN with the acquired image phantom data, 4D arrays containing all waveform pairs for each detector line-of-response were input to the CNN. The predicted TOF values output from the CNN were used to generate dPEI images. None of the data used to train the CNN was subsequently reused to determine the timing resolution in Fig. 2b,c or for the imaging data in Fig. 4.

Image generation and post processing

The dPEI setup consists of two single-channel CRI-MCP-PMT detectors, therefore the cross-sectional 2-D image was obtained by building up the dPEI image one row at a time - acquiring a timing spectrum at each x-position (Fig. 3) with the collimation and step size described in the "Datasets" section. At each x-position, the time-of-flight difference ($t_A - t_B$) of each coincidence event was determined by the CNN method and directly converted to the spatial image domain (without a reconstruction algorithm) using the following equation:

$$y = \frac{c \times (t_A - t_B)}{2}$$

(Eq. 1)

where c is the speed of light, and y is defined relative to the mid-point of the line-of-response (Fig. 3b). The computed y-positions were histogrammed to form one image row (Fig. 3b,c) with a bin size of 1-mm for the dPEI images of the image quality phantom and the spatial resolution test phantom or a bin size of 4-mm for the brain phantom image. The concatenation of all single row images generates the 2-D dPEI images as shown in Fig. 3d.

As described above, dPEI images were generated directly from the measured data without any reconstruction. Subsequently, the image was corrected for attenuation of the 511 keV photons. The probability that both 511-keV photons will reach the detector, P_{det}, is given by:

$$P_{det} = \sum_i e^{-\mu_i L_i}$$

(Eq. 2)

where L_i is the length traversed through material i, and μ_i is the linear attenuation coefficient of material i at 511 keV, which was taken as 0.0969 cm^{-1} for water and 0.1120 cm^{-1} for acrylic. The correction is carried out through manual segmentation of each material type in the non-attenuated corrected dPEI image[27]. It was assumed that the NEMA NU-4 image quality phantom (except the air-filled void) and the brain phantom were uniformly filled with water, and that the spatial resolution test phantom was a uniform acrylic disk. The attenuation corrected image of the Hoffman brain phantom is shown in Supplementary Data Fig. 4b. No correction for accidental coincidences or scattered coincidence events were made, as the contribution of these events in this experimental geometry was determined to be negligible.

After attenuation correction, Gaussian smoothing and image up-scaling were performed to average and interpolate the local pixel values for improved visual representation, reducing the effect of pixel-to-pixel variation. A sigma value of 1.4 pixels (= 1.4 mm) was used for the image quality phantom and the spatial resolution test phantom, and a sigma value of 0.8 pixel (= 3.2 mm) was used for the brain phantom. The same 4-fold up-sampling with bicubic interpolation was performed for all images. Supplementary Data Figs. 4c,d show the images after the Gaussian smoothing and rescaling, respectively.

Extended Data
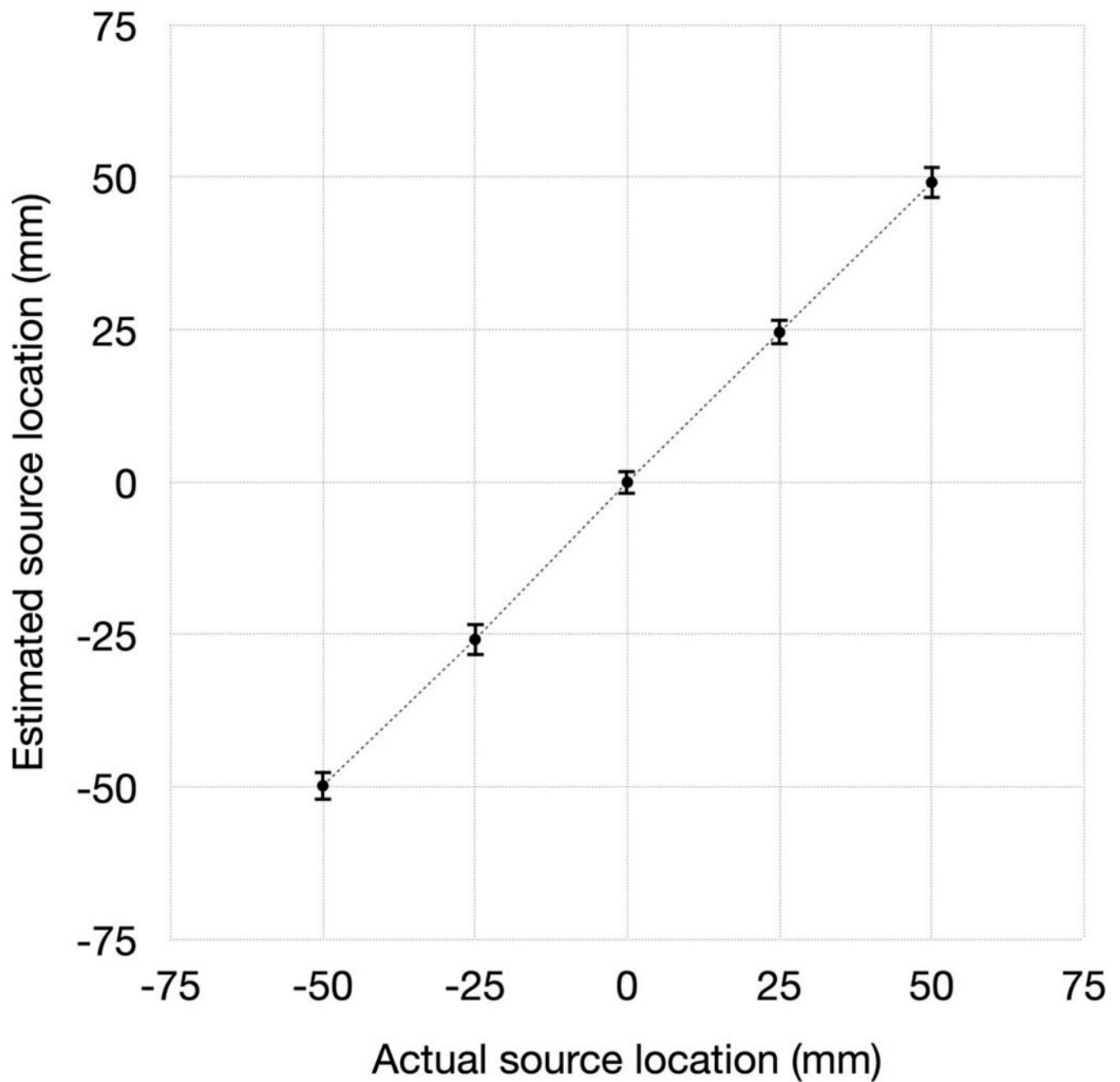
Extended Data Fig. 1. Accuracy of source localization based on measured timing difference.
Location of a radioactive point source as determined by the timing difference t_A-t_B (Eq.
1) versus the known location of the source, across a distance of 10 cm, using the data in
Fig. 2c. Error bar represents ± (FWHM of the distribution at each location ÷ 2). The source
location is accurately determined over the entire range.
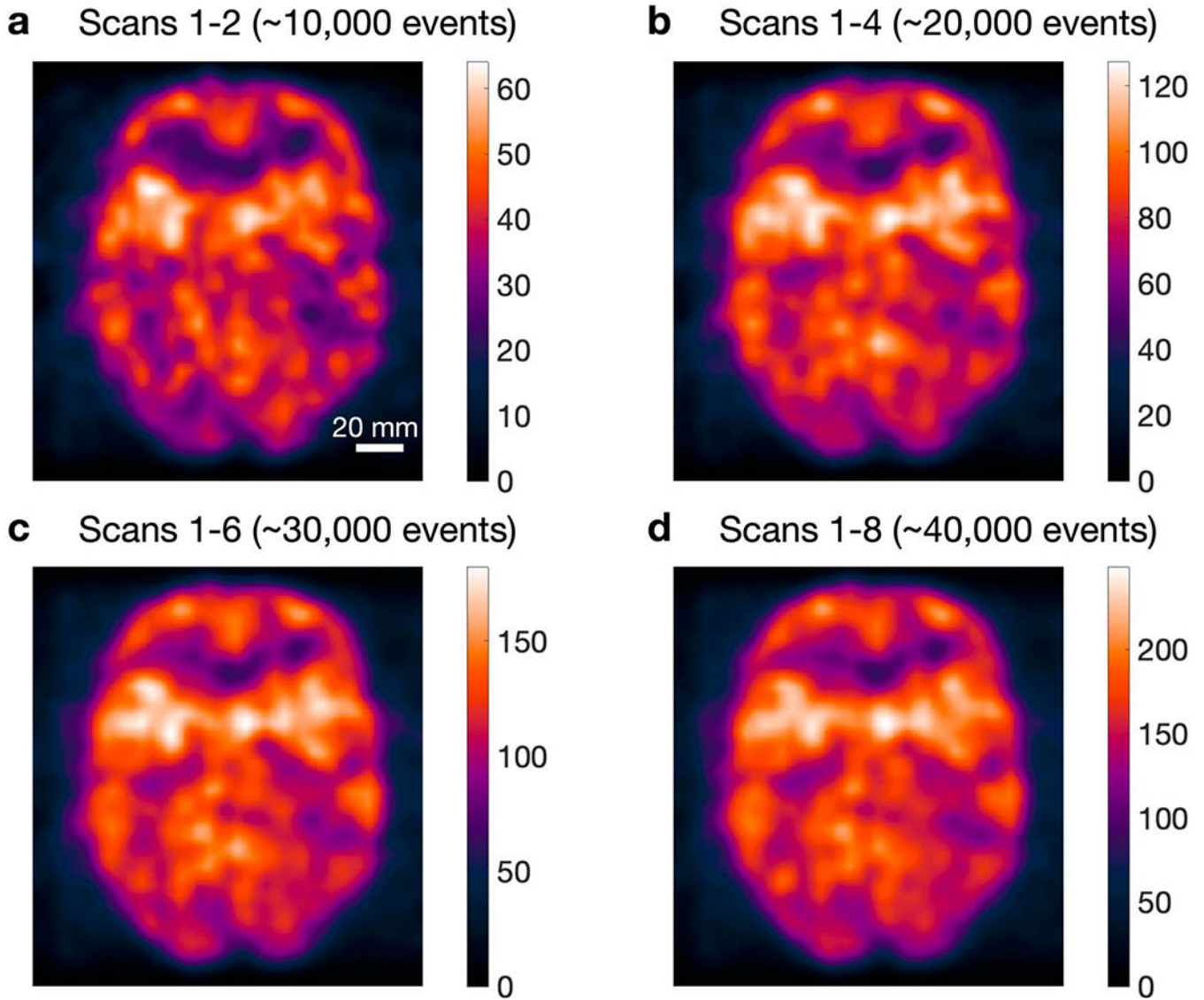
Extended Data Fig. 2. Effect or number nf detected events tin dPEI images.
dPEI images of the 2-D Hoffman brain phantom generated using a different number of
events: **a,** ~10,000 events, **b,** ~20,000 events, **c,** ~30,000 events, and **d,** ~40,000 events. Each
acquisition was performed over 44 different *x*-positions (4-mm intervals) and each scan took
a total of 6 hours and used ~850 MBq (~23 mCi) of ^{18}F-FDG activity. All images were
post-processed (analytical attenuation correction, Gaussian smoothing (σ=0.8), and 4-fold
up-sampling) as shown in Extended Data Fig. 6. This image demonstrates the relatively
modest number of detected events needed to form an image of a slice representing the
human brain, with little improvement above 20,000 events.

Supplementary Material

Refer to Web version on PubMed Central for supplementary material.

Acknowledgments:

References

1. Clackdoyle R & Defrise M Tomographic Reconstruction in the 21st Century. IEEE Signal Proc. Mag 27, 60–80, doi:10.1109/msp.2010.936743 (2010).

2. Lange K & Carson R EM reconstruction algorithms for emission and transmission tomography. J. Comput. Assist. Tomogr 8, 306–316 (1984). [PubMed: 6608535]

3. Wright GA Magnetic resonance imaging. IEEE Signal Proc. Mag 14, 56–66, doi:10.1109/79.560324 (1997).

4. Lecoq P et al. Roadmap toward the 10 ps time-of-flight PET challenge. Phys. Med. Biol 65, 21RM01, doi:10.1088/1361-6560/ab9500 (2020).

5. van Sluis J et al. Performance Characteristics of the Digital Biograph Vision PET/CT System. J. Nucl. Med 60, 1031–1036, doi:10.2967/jnumed.118.215418 (2019). [PubMed: 30630944]

6. Budinger TF Time-of-flight positron emission tomography: status relative to conventional PET. J. Nucl. Med 24, 73–78 (1983). [PubMed: 6336778]

7. Schaart DR Physics and technology of time-of-flight PET detectors. Phys. Med. Biol 66, 09TR01, doi:10.1088/1361-6560/abee56 (2021).

8. Lecoq P et al. Factors influencing time resolution of scintillators and ways to improve them. IEEE Trans. Nucl. Sci 57, 2411–2416, doi:10.1109/TNS.2010.2049860 (2010).

9. Nemallapudi MV, Gundacker S, Lecoq P & Auffray E Single photon time resolution of state of the art SiPMs. J. Inst 11, P10016–P10016, doi:10.1088/1748-0221/11/10/p10016 (2016).

10. Cates JW, Gundacker S, Auffray E, Lecoq P & Levin CS Improved single photon time resolution for analog SiPMs with front end readout that reduces influence of electronic noise. Phys. Med. Biol 63, 185022, doi:10.1088/1361-6560/aadbcd (2018). [PubMed: 30129562]

11. erenkov PA Visible radiation produced by electrons moving in a medium with velocities exceeding that of light. Phys. Rev 52, 378–379, doi:10.1103/PhysRev.52.378 (1937).

12. Jelley JV Cerenkov radiation and its applications. Br. J. Appl. Phys 6, 227–232, doi:10.1088/0508-3443/6/7/301 (1955).

13. Korpar S, Dolenec R, Križan P, Pestotnik R & Stanovnik A Study of TOF PET using Cherenkov light. Nucl. Instrum. Methods Phys. Res. A 654, 532–538, doi:10.1016/j.nima.2011.06.035 (2011).

14. Brunner SE, Gruber L, Marton J, Suzuki K & Hirtl A Studies on the Cherenkov effect for improved time resolution of TOF-PET. IEEE Trans. Nucl. Sci 61, 443–447, doi:10.1109/TNS.2013.2281667 (2014).

15. Kwon SI, Gola A, Ferri A, Piemonte C & Cherry SR Bismuth germanate coupled to near ultraviolet silicon photomultipliers for time-of-flight PET. Phys. Med. Biol 61, L38–L47, doi:10.1088/0031-9155/61/18/L38 (2016). [PubMed: 27589153]

16. Kume H, Koyama K, Nakatsugawa K, Suzuki S & Fatlowitz D Ultrafast microchannel plate photomultipliers. Appl. Optics. 27, 1170–1178, doi:10.1364/AO.27.001170 (1988).

17. Ota R et al. Coincidence time resolution of 30 ps FWHM using a pair of Cherenkov-radiator-integrated MCP-PMTs. Phys. Med. Biol 64, 07LT01, doi:10.1088/1361-6560/ab0fce (2019).

18. Ota R et al. Lead-free MCP to improve coincidence time resolution and reduce MCP direct interactions. Phys. Med. Biol 66, 064006, doi:10.1088/1361-6560/abea2c (2021). [PubMed: 33636710]

19. Berg E & Cherry SR Using convolutional neural networks to estimate time-of-flight from PET detector waveforms. Phys. Med. Biol 63, 02LT01, doi:10.1088/1361-6560/aa9dc5 (2018).

20. Hendee WR Cross sectional medical imaging: a history. RadioGraphics 9, 1155–1180, doi:10.1148/radiographics.9.6.2685939 (1989). [PubMed: 2685939]

21. Jan S et al. GATE V6: a major enhancement of the GATE simulation platform enabling modelling of CT and radiotherapy. Phys. Med. Biol 56, 881–901, doi:10.1088/0031-9155/56/4/001 (2011). [PubMed: 21248393]

22. Sarrut D et al. Advanced Monte Carlo simulations of emission tomography imaging systems with GATE. Phys. Med. Biol, 66, 10TR03, doi:10.1088/1361-6560/abf276 (2021).

23. Ota R et al. Precise analysis of the timing performance of Cherenkov-radiator-integrated MCP-PMTs: analytical deconvolution of MCP direct interactions. Phys. Med. Biol 65, 10NT03, doi:10.1088/1361-6560/ab8c8f (2020).

24. NEMA Standards Publication NU 4–2008. Performance measurements of small animal positron emission tomographs (National Electrical Manufacturers Association, 2008).

25. LeCun Y, Bengio Y & Hinton G Deep learning. Nature 521, 436–444, doi:10.1038/nature14539 (2015). [PubMed: 26017442]

26. He K, Zhang X, Ren S & Sun J in 2016 IEEE Conference on Computer Vision and Pattern Recognition (CVPR) 770–778 (2016).

27. D'Ambrosio D, Zagni F, Spinelli AE & Marengo M Attenuation correction for small animal PET images: a comparison of two methods. Comp. Math. Methods. Med 2013, 103476, doi:10.1155/2013/103476 (2013).

28. Berg E, Kwon SI, Ota R, & Cherry SR Waveform data for direct positron imaging, Dryad, Dataset, doi:10.25338/B89623 (2021).
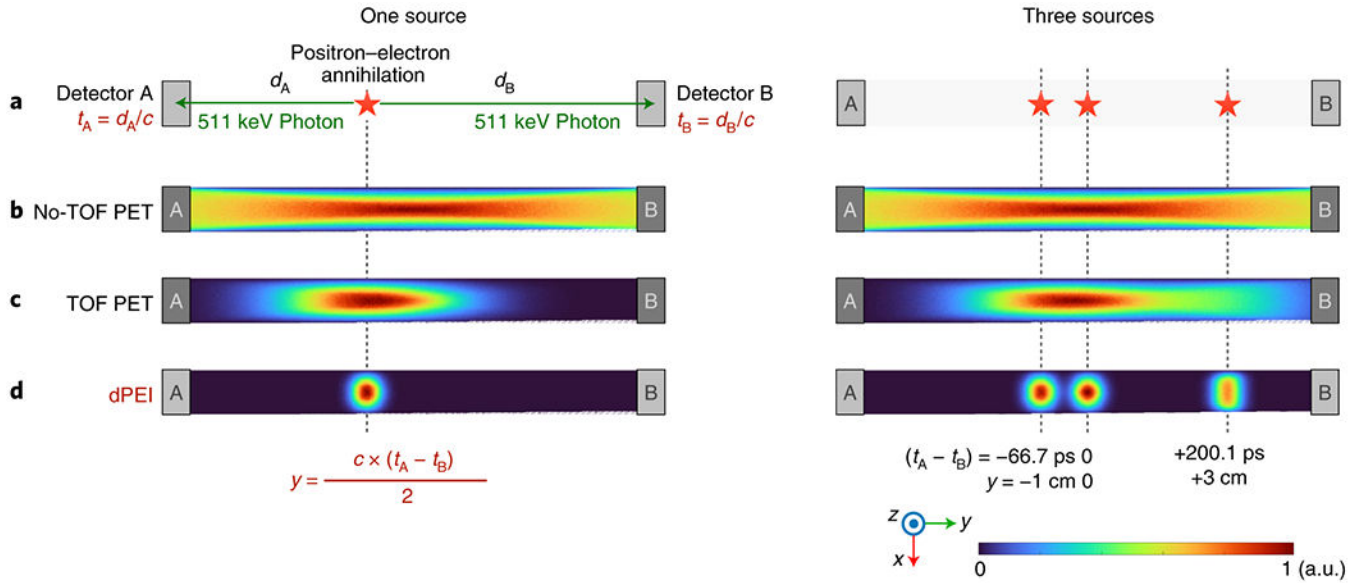
Fig. 1: Basis for direct imaging of positron-emitting radiotracers using ultra-fast timing.
a, Detection of back-to-back annihilation photons by a pair of radiation detectors and the source location-dependent arrival times of the two photons. **b,** Simulations showing the probability distribution of source locations for a detected event (9.6×9.6 mm^2 detector area, detector separation = 96 mm) in conventional PET imaging where no timing information is available. When multiple sources are present (right hand side), it is not possible to discriminate them without additional measurements from different detector orientations. **c,** partial localization when time-of-flight (TOF) information is added (example shown is 210 ps timing resolution, corresponding to 3.15 cm spatially); **d,** Direct PEI, the new modality, in which the timing resolution of 32 ps allows the event to be localized within 4.8 mm, providing the basis for direct image generation without image reconstruction. The three sources can now be clearly resolved from a single measurement. The 2-D sensitivity maps presented are computed by simulation using the stated geometry and are calculated by integrating the 3-D distributions across the detector width perpendicular to the figure. The lower intensity and vertical elongation of the source located at +3 cm reflects the geometric response of coincidence detection for a pair of rectangular detectors.
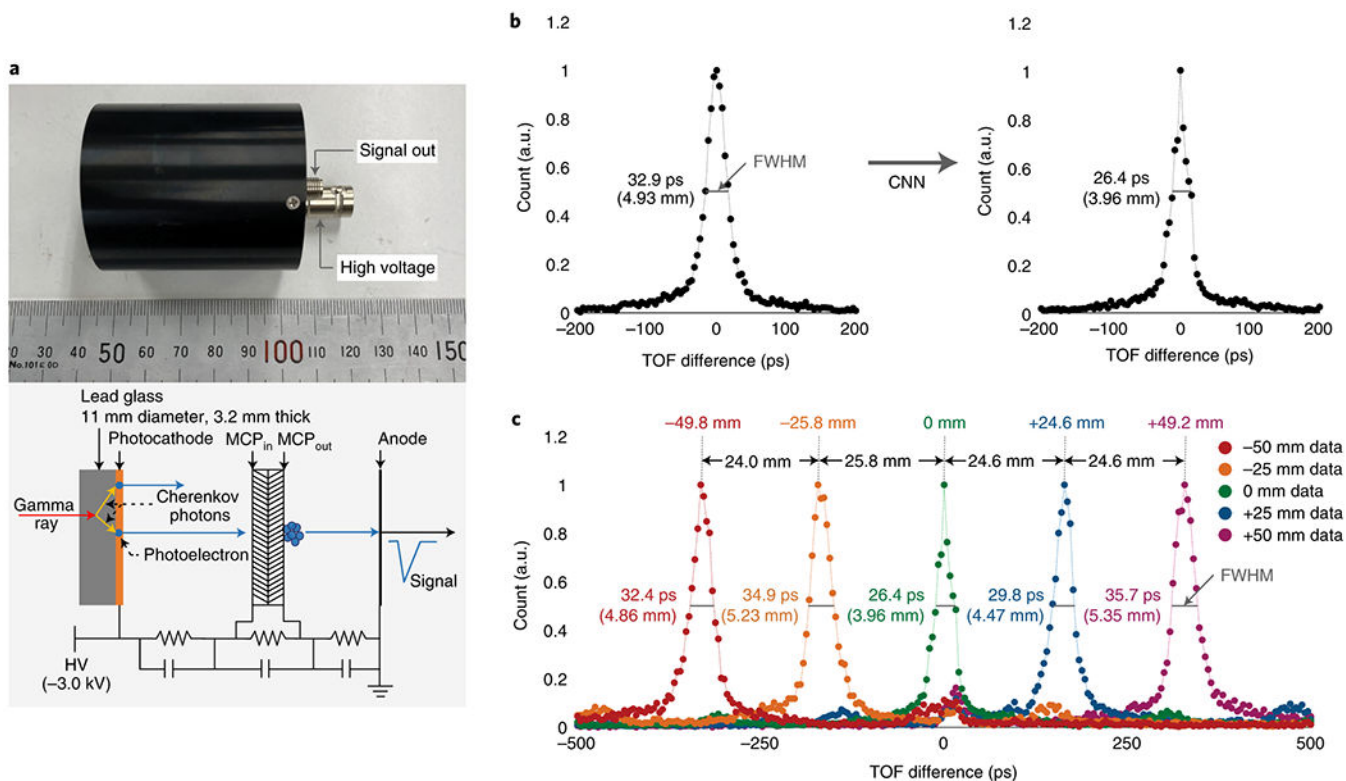
Fig. 2: Timing resolution of 32 ps measured with MCP-PMT radiation detectors.
a, Photograph and schematic of the microchannel plate photomultiplier tube (MCP-PMT) with an integrated lead-glass Cerenkov radiator as its entrance window, allowing Cerenkov radiation to reach the photocathode and liberate electrons without any intervening optical barriers. The MCP structure also is modified to remove lead compounds to reduce direct interactions of 511 keV annihilation photons in the structure itself; **b,** Histogram of time-of-flight differences measured from two MCP-PMTs with integrated Cerenkov radiators in coincidence for a centrally-located ^{22}Na point source. The MCP-PMT signals are digitized at 50 giga-samples-per-second, and the timing pick off determined by applying constant fraction discrimination in software. Using a convolutional neural network to estimate the time-of-flight difference of the waveforms further improves the timing resolution from 32.9 ps to 26.4 ps; **c,** Histograms of time of flight differences as the point source is moved between the two detectors in steps of 2.5 cm, showing the linear relationship with source location. The calculated source location based on the timing difference is shown and is within 0.8 mm of the actual location. The timing resolution varied between 26.4 and 35.7 ps across the 10 cm range studied. The average timing resolution across the range was 32 ps. The timing resolution was measured as the full width at half maximum (FWHM) of the timing distributions.
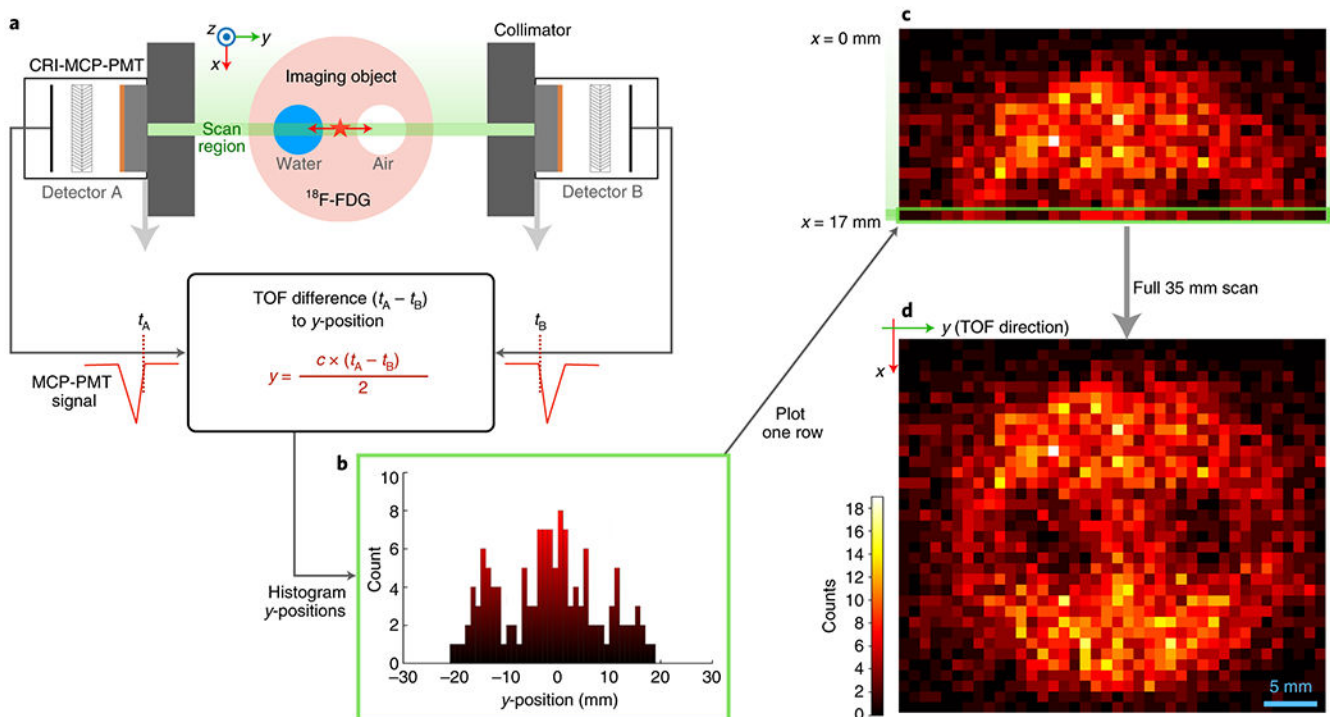
Fig. 3: Acquiring a cross-sectional image using a pair of CRI-MCP-PMT detectors.
a, The x-direction of the image is encoded by the position of the collimated detector pair, and the y-direction is encoded by the timing information as shown in Fig. 2D. The test object is filled with the radiotracer ^{18}F-fluorodeoxyglucose (^{18}F-FDG), except for two voids (one air and one water); **b,** Data is acquired for each x-position of the detector pair and the timing information used to determine the distribution of activity along the line between the two detectors; **c,** The image is built up line by line as the detectors are translated. The image resolution in the x direction is governed by the opening of the collimator, and in the y-direction by the timing resolution of the detector pair; **d,** The final raw image.
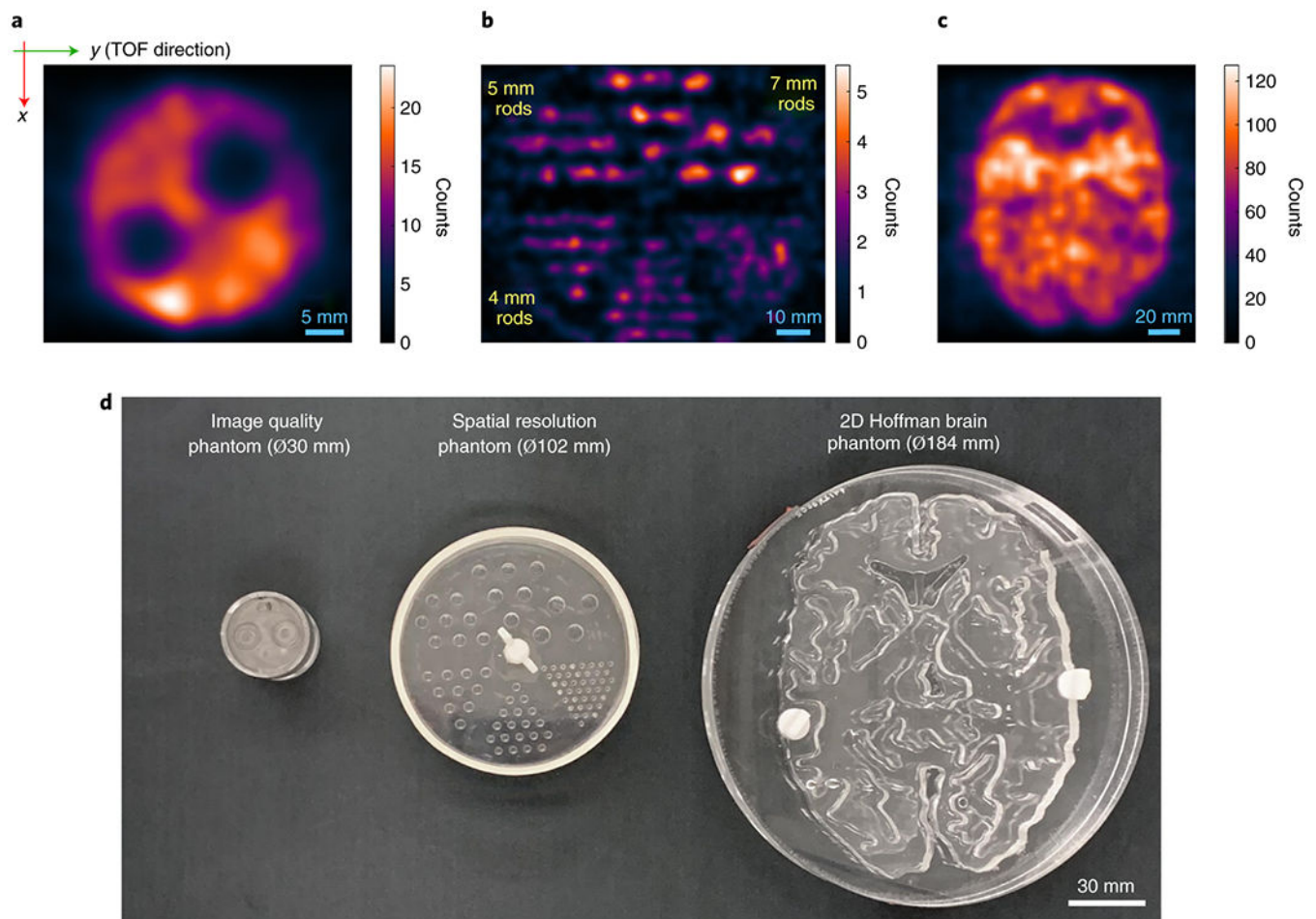
Fig. 4: Cross-sectional images for different scale objects directly measured from a single angular view and without image reconstruction.

Images were acquired with the dPEI set up illustrated in Fig. 3. Corrections for radioactive decay, acquisition time, geometric sensitivity and photon attenuation have been applied to the raw image data; **a,** Image quality test object with 8 mm diameter air and water-filled voids; **b,** Structured object with an array of sources of different sizes and spacing to illustrate spatial resolution. In both **a** and **b**, objects were imaged with a detector spacing of 20 cm, a collimator opening of 2 mm by 10 mm (the latter defining the imaging slice thickness) and the detectors were translated by 1 mm to ensure sufficient sampling in the x-direction. The y-direction was sampled in 6.67 ps increments, also corresponding to 1 mm. **c,** The detectors were moved further apart (30 cm) and the collimation opened up to 8 mm by 10 mm to scale up to an object size with dimensions relevant to human imaging. dPEI images of the 2-D Hoffman brain phantom representing the distribution of ^{18}F-FDG in a slice of the human brain acquired with 4 mm step size. **d,** Corresponding photograph of the test objects showing dimensions. For details see methods.